Spatially resolved and observer-free experimental quantification of spatial resolution in tomographic images

Spatially-resolved and observer-free experimental quantification of spatial resolution in tomographic images

S. A. Tsekenis[1], N. Tait[2], H. McCann[1]

[1]*School of Engineering, The University of Edinburgh, Edinburgh, EH9 3JL, United Kingdom*

[2]*Shell U.K. Limited, Shell Centre, London, SE1 7NA, United Kingdom*

We present a novel framework and experimental method for the quantification of spatial resolution of a tomography system. The framework adopts the 'black box' view of an imaging system, considering only its input and output. The tomography system is locally stimulated with a step input viz. a sharp edge. The output, viz. the reconstructed images, are analysed by Fourier decomposition of their spatial frequency components, and the local limiting spatial resolution is determined using a cut-off threshold. At no point is an observer involved in the process. The framework also includes a means of translating the quantification region in the imaging space, thus creating a spatially-resolved map of objectively-quantified spatial resolution. As a case-study, the framework is experimentally applied using a gaseous propane phantom measured by a well-established Chemical Species Tomography (CST) system. A spatial resolution map consisting of 28 regions is produced. In isolated regions the indicated performance is 4-times better than that suggested in literature and varies by 57% across the imaging space. A mechanism based on adjacent but non-interacting beams is hypothesised to explain the observed behaviour. The mechanism suggests that, as also independently concluded by other methods, a geometrically regular beam array maintains maximum objectivity in reconstructions. We believe that the proposed framework, methodology and findings will be of value in the design and performance evaluation of tomographic imaging arrays and systems.

I. INTRODUCTION

A. General statement for field of study

The term "spatial resolution" frequently appears in literature concerning tomographic imaging systems. In this context, a projection is defined as the shadow cast by the measured subject when the latter is viewed from a specific angle. In broader terms, as well as in this paper, a projection is defined as a single or group of measurements performed at a specific view angle. The concept of spatial resolution has been comprehensively studied in medical tomography applications that are typically characterised by a relatively large number of projections and slow acquisitions. On the other hand, in industrial process tomography applications which are characterised by relatively fast acquisitions and a smaller number of projections, the concept of spatial resolution has not been studied as thoroughly. Nonetheless, spatial resolution is of paramount importance in industrial process applications as it relates to the smallest features that can be detected and thereby the suitability of a tomographic modality and system for a given application. Hence, a quantitative knowledge of spatial

resolution facilitates the interpretation and exploitation of tomographic images. This paper proposes a method to determine quantitatively the spatial resolution of tomographic imaging systems that use small numbers of measurements.

B. Defining spatial resolution

Historically the term 'spatial resolution' was introduced to describe the resolving power of a purely optical, non-tomographic imaging system.[1,2] In optical image-forming devices the term is synonymous with the angular resolution of the system, i.e. the ability of the system to resolve image features with a small angular separation.[3]

In tomographic applications the optics definition is inapplicable as the image is formed synthetically. Nevertheless, the term has been used in conjunction with what seemingly are manifestations of the finite spatial resolution of the imaging system such as: the sharpness of the reconstructed image[4], the smallest structure that can be detected in the image[5] and the ability to tell two objects apart[6]. Other older examples of usage of the term exist[7].

The apparent loose usage of the term requires a broad definition to be established early in a given work. We define spatial resolution as "a measure of the ability of the holistic imaging system and its operator to distinguish physically non-overlapping features anywhere inside the image space of an acquired or reconstructed image".

It is worth making a distinction between spatial and contrast resolution, the latter referring to the ability of the imaging system to resolve two features separated by a distance larger than the spatial resolution and progressively decreasing differential intensity.

C. Accumulative degradation of spatial resolution

A tomography system is composed of four fundamental functional stages: tomographic measurement modality, data acquisition system, image reconstruction algorithm and any additional processing, and data presentation[8]. Other systems might be composed of fewer stages. Imperfections encountered in each stage have a detrimental impact on the spatial resolution of the system. We present examples of imperfections in each functional stage.

The imaging measurement modality defines the sensors employed to acquire the raw data from the imaging space. For direct inversion an infinite number of measurements at an infinite number of angles are required. However, in practical applications and process tomography in particular, the number of measurements is limited by the number of sensors that can be placed around the imaging space due to physical obstructions.

In the case of hard-field tomography, the sensors used have a finite sensitive area thus spatial averaging of the ray-sums is unavoidable. The effect is much less well defined in soft-field tomography such as Electrical Capacitance Tomography (ECT) since the measurements are sensitive, in principle, to all parts of the subject, but the finite area of the excitation electrode-pairs will also result in spatial averaging of the electric fields.

Noise introduced by the imaging modality will also be present in the initial measurements. For example, in the case of Cone-Beam CT (CBCT) noise can take the form of light or scatter radiation from sources other than the X-ray generator[6]. With in-cylinder N-IR Chemical Species Tomography (CST) where LASER light is guided with fibre optics, cladding modes can be modulated randomly by minute vibration of the fibres and manifest as measurement noise, the amplitude of which can be comparable with the useful signal[9]. Temperature gradients along the imaging space introduce beam steering which, coupled with the received intensity profile at the detector, introduces noise. Photometry of the transmitted light is typically performed using transimpedance amplifiers where the requirement for bandwidth in high speed applications and low total output noise are contradictory design objectives[10].

Selection of an appropriate image reconstruction algorithm for the target application is critical to the spatial resolution of the reconstructed images[11]. Simple image reconstruction algorithms based on the Filtered Back-Projection (FBP) technique can provide sufficiently accurate reconstructions only when the number of available projections is large.

However, the small number of measurements available from sparse imaging arrays greatly exacerbates the ill-posed and ill-conditioned nature of the data inversion problem[12]. In extreme cases, the use of a priori information (e.g. non-negativity, smoothness, feature shape) is necessary to regularise the solution[9]. However, caution must be exercised when incorporating a priori information in the image reconstruction as, depending on the application's requirements, they could detract from the objectivity of the measurements.

Finite-Element Modelling (FEM) simulations of the physical process may also be used to steer the inversion process. If the models developed are known to be accurate, the experimental measurements are limited to signalling deviations from the behaviour anticipated by simulation. In this case, point measurements might be sufficient for automated process control. However, in practice, tomography is applied to further our understanding of the physical processes involved and the validation of the mathematical models that describe them. Consequently, the improvement in spatial resolution by incorporating theoretical models and a priori information into the image reconstruction algorithm is limited and should be weighed against the increase in complexity in a given application.

The last stage of the system is the presentation and interpretation of the image reconstruction results. This task is commonly performed by a viewer, nevertheless a machine can also be made to interpret the results and control a process[8,45]. An example of closed-loop control has been reported using Electrical Impedance Tomography (EIT) to measure and control the injection of concentrate in a fluid flow.

When the images are displayed to a viewer, judgment of the displayed images is highly subjective and depends on the viewer's experience, prior knowledge of the subject, expectations, colour sensitivity, resolution of the displayed image and visual acuity. Common pathological conditions will introduce distortions[13,14]. The colour palette used (e.g. ironbow, blue-red, high contrast, grayscale) can also influence the viewer's judgment.

The spatial resolution of a tomography system is affected by a plethora of factors at each tomographic stage. The contribution of each factor to the final spatial resolution is complex.

D. Approaches to the study of spatial resolution

Literature on tomography systems contains numerous approaches for the quantification, as well as prediction and optimisation of the spatial resolution performance of a tomography system.

1. Visual comparison of imaging performance

The first and simplest approach to quantify spatial resolution is the visual assessment of reconstructed images. In one study[15] flame chemiluminescence was imaged using CT. The spatial resolution was tested by the introduction in the imaging space of simulated, noise-free unidirectional cosine waves of varying spatial frequency. The reconstructions were visually inspected to determine the appearance of aliasing, which signified that the limiting spatial resolution had been reached. In another case, visual assessment of reconstructed images was also employed in an extensive comparison of CBCT scanners in terms of their spatial resolution[16]. The phantom used was a standard solid polymethyl-methacrylate (PMMA) cylinder with slots for test inserts. Two test inserts were used; one with line-pair features and one with cylindrical rod features. Both inserts had varying feature sizes. The quality of the reconstructions from both inserts was evaluated, using a scorecard, by four observers from two different medical backgrounds.

2. Synthetic figure of merit imaging performance comparisons

The second approach identified is the introduction of a figure of merit to describe the 'reconstruction quality'. In one example[17], reconstructions were performed of simulated and experimental methane concentrations. A turbulent methane distribution was initially simulated in the cross section of a duct. Reconstruction parameters such as the number of projections, beams per projection, and number of pixels in the solution were optimised by brute-force sweeping across a search space. Subsequently an experimental coaxial flow of methane/air was tomographically imaged using IR absorption. In the experimental studies, 6 projections

of 25 beams each and a fixed reconstruction grid of 11x11 pixels were used. The discrepancy between the actual and reconstructed distributions was described by a spatially averaged error, defined as the sum of the correlation between each pixel in the phantom and the corresponding pixel in the reconstruction. However, the resulting spatially averaged error is a single scalar quantity for the entire imaging space.

3. Heuristic optimisations of beam array geometry

The third approach aims to optimise the beam array geometry by more uniformly distributing the available beams in the imaging space, thereby improving its sampling. Subsequently, image reconstructions of fixed concentration distributions are, similarly to the first approach, heuristically compared to infer the gross spatial resolution of the system. In one example[12], a regular 32-beam array developed for an IC engine CST application was revised by reducing the number of beams to 27 and re-arranging them for more extensive coverage of the sinogram space.

The theoretical underpinning of this heuristic approach has been previously studied[18,19] by application of the Sampling Theorem in two dimensions. In the case of a circular imaging space of diameter D, the spatial resolution δ_x of a tomographic system can be linked to the number of projections m [20] as follows:

$$\delta_x \approx \frac{\pi D}{m} \tag{1}$$

However, contrary to theoretical estimates, practical studies involving phantoms have shown that the spatial resolution experimentally obtained is in fact better than that predicted by equation 1. Cases of 8-times[21] and 5-times[22] improvement have been reported. An improvement factor of π has been proposed[7].

4. Rigorous optimisations of beam array geometry

The fourth approach aims to improve the resulting spatial resolution using a rigorously defined process. For example, resolution matrices can be used to characterise the reconstruction penalty incurred when prior information (e.g. smoothness) is included in the reconstruction process in order to regularise the solution. In one case[23] the mathematical properties of the resolution matrix - a function of the beam array geometry - are analysed in the context of a limited-views tomography system. A fitness function is then derived and used to predict the "*reconstruction error*" (RE). For a given number of beams, the fitness function is optimised to yield the minimum RE. The work carefully avoids the use of spatial resolution as a figure of reconstruction performance per se. However, the work is of relevance as the RE, a scalar value, is defined in the work as the normalised difference between the actual and reconstructed subjects. As such, minimisation of the RE must require minimisation of the errors leading to deterioration of the spatial resolution.

5. Quantification using the Line Spread Function (LSF)

In this approach of quantifying spatial resolution a thin line feature is typically introduced in the imaging space and reconstructed as experimental a plot of image intensity with distance along the vector, resulting in a bell-shaped curve. The Full-Width Half-Maximum (FWHM) figure from this curve is then used.

The LSF/FWHM combination has been applied numerous times in literature, particularly in medical diagnostic instruments that have a sufficiently large number of views to adequately resolve a line feature. The spatial resolution of Positron Emission Tomography (PET) scanners was evaluated[24,25] using a radioactive line source which was translated in the imaging space. In a clinical evaluation of PET image reconstruction[26] it was stated that the FWHM can be used to determine the system's spatial resolution. However, evaluation of reconstructed images in the study was performed by observation of the "overall image quality" and the number of distinguishable features of interest.

The LSF of the system need not be evaluated directly. In one example[27] using cold neutron tomography, a sharp-edged sheet of Gadolinium was reconstructed, yielding the Edge Spread Function (ESF). Subsequently, the ESF was differentiated with respect to intensity to produce the LSF. Instead of measuring the FWHM or analyzing the frequency components (see next approach), the linear distance over which the intensity increases from 10% to 90% (spatial equivalent of 'rise-time') was used as the figure of spatial resolution. The shape of the LSF was used to extract information about the source of image degradation.

6. Quantification using the Modulation Transfer Function (MTF)

In this approach a sharp-edged feature is introduced in the imaging space and reconstructed as normal. Similarly to the FWHM method, the pixel intensity along a vector perpendicular to the edge is plotted, but a step-shaped curve is produced instead. Fourier decomposition of the step signal yields the MTF of the system at that position, describing how spatial frequencies are attenuated by the tomography system.

In one case[4], similarly to[28], a gold leaf edge was introduced in a X-ray scanner and reconstructed. The MTF was computed and the spatial resolution determined by applying a 10% cut-off threshold to the MTF. The gold edge was not translated in the imaging space. In another case[5], instead of an artificial sharp-edge, bone specimens with well-characterised features were placed in an X-ray scanner. The MTF was computed and a 10% intensity cut-off applied, however the spatial resolution was evaluated as the reciprocal of two-times the spatial frequency component at the cut-off point.

E. Focus of this paper

All spatial resolution quantification approaches described thus far have particular strengths and weaknesses. Still, no single method has been reported that combines all the strengths. The focus of this paper is to develop

and present a method that is simultaneously rigorous, objective and offers spatially-resolved quantification of spatial resolution while capturing noise sources present in the implemented tomography system. Whilst the proposed method has been inspired by sparse tomography systems, it should be noted that it ought to apply in general to all systems.

II. SPATIAL RESOLUTION QUANTIFICATION METHOD

A. The 'black-box' tomography system

The performance of a tomography system is ultimately judged solely from the reconstructed images when prior knowledge about the subject imaged is available. That is to say, the tomographic system in its entirety is treated as a 'black box'. As such, the input to the system is the actual subject to be tomographically imaged and the output is the reconstructed image. This analogy disassociates the means of creating tomographic images (e.g. choice of inversion algorithm) from the images themselves and allows them to be examined independently.

B. Spatial frequency content of reconstructed images

Tomographic reconstructions are 2-dimensional functions $f(x,y)$ in spatial coordinates (x,y) on an image plane. Each function describes how colours or grayscale values (intensities, or brightness) vary in space. Nowadays the images are processed and displayed digitally, therefore the intensity functions are discretised. As such, the spectral content (spatial frequency components or monotones) of any 2-dimensional image of PxP pixels can be described by the 2-dimensional Discrete Fourier Transform (DFT)[29] as follows:

$$F(u,v)=\sum_{x=0}^{P-1}\sum_{y=0}^{P-1} f(x,y)e^{\frac{-j\pi(ux+vy)}{P}} \tag{2}$$

where u and v are the contributions of the spectral components in the x and y direction respectively. The spectral components themselves are simple images in the spatial domain thus complex images can be represented by summation of these basis images. Finally, the amplitude and phase of the spatial frequency components constitute the amplitude $|F(u,v)|$ and phase $\varphi(u,v)$ spectra, respectively.

C. Filtering of special frequency components – the MTF

Imaging system imperfections as described in section I.C act to filter the special frequency content of an image, the resulting tomographic image having a spatial frequency content denoted $\hat{F}(u,v)$. The filtering action, in general, can be described by its frequency-domain transfer function $H(u,v)$ and the filtered tomographic image as given by equation (3):

$$\hat{F}(u,v) = F(u,v)H(u,v) \tag{3}$$

The net effect of imperfections in the imaging system can be described by the system's response to an ideal point being imaged. The filtering function $H(u,v)$ is then the 2-D DFT of the system's Point Spread Function (PSF). The DFT of the PSF is defined as the system's MTF[30]. The MTF functionally describes the deviation of the tomographically produced imaged from the actual image of the subject imaged as follows:

$$H(u,v) = DFT(PSF) = MTF = \frac{\hat{F}(u,v)}{F(u,v)} \tag{4}$$

Most importantly, the MTF encompasses all phenomena contributing to deterioration of the reconstructed image. Consequently the spatial resolution of an imaging system can be described solely through its MTF. The MTF of the imaging system is not known from first principles, but can be measured.

D. Alternative definition of the MTF

The intensity MTF or MTF_I of a tomography system is defined[31] as the transfer of the intensity modulation from the physical domain M to the reconstructed image domain $\hat{M}$ as shown in equation (5):

$$MTF_I = \frac{\hat{M}}{M} = \frac{\dfrac{\hat{I}_{\max} - \hat{I}_{\min}}{\hat{I}_{\max} + \hat{I}_{\min}}}{\dfrac{I_{\max} - I_{\min}}{I_{\max} + I_{\min}}} \tag{5}$$

where $\hat{I}_{\max}, \hat{I}_{\min}, I_{\max}, I_{\min}$ are the maximum and minimum intensities present in the reconstructed image and physical domains respectively.

The two definitions given by equations (4) and (5) are not mathematically equivalent as *MTF* contains amplitude and phase information, whereas MTF_I only amplitude. A distinction can be made by defining equation (4) as the Optical Transfer Function (*OTF*) and equation (5) as the *MTF*[31]. In that case the *OTF* is given by equation (6) as follows:

$$OTF = MTF_I e^{j\varphi(u,v)} \tag{6}$$

where the imaginary term is the Phase Transfer Function (PTF), thereby restoring phase information.

The human eye is sensitive only to the spatial variation of the resultant intensity as described by equation (5). Therefore, considering the modulation depth of the resultant intensity to quantify spatial resolution is a valid, yet insufficient method as discussed in the following section.

E. Association of MTF definitions - achieving objectivity

The quantification of spatial resolution by evaluation of the intensity transfer from the physical domain to the reconstructed image domain (as described by equation 5) is not sufficiently objective, as only visual perception is involved. On the other hand, quantification by evaluating transfer of the complex components of the *MTF* (as described by equation 4) is unintuitive.

The two definitions can be unified[32] by graphically examining the effect that a simplified non-unity MTF in equation (4) has on equation (5). Fig. 1 depicts a single spatial frequency in the physical domain with spectral components F and intensity modulation M. The intensity I shown below the image has larger amplitude for darker pixels and is therefore spatially varying. The spatial frequency is captured by the imaging system and represented as a spatial frequency of spectral component $\hat{F}$ and intensity modulation $\hat{M}$.

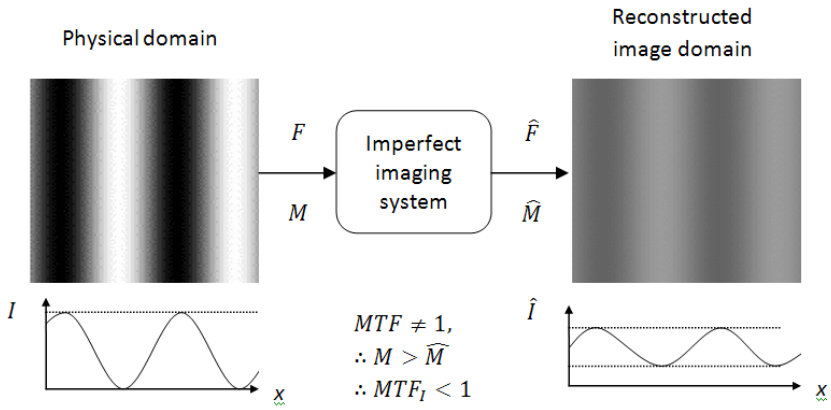

FIG. 1: The effect of imperfect imaging system on a single spatial frequency component.

The MTF of the imaging system will not be equal to unity as, due to the imperfect imaging system, the input and output spectral components are not equal. Assuming that the phase spectra of the input and output are equal, i.e. $\hat{\phi} = \phi$, equation (7) then follows:

$$MTF = |MTF| = MTF_I \quad \text{for } \hat{\phi} = \phi \tag{7}$$

The subject representation by the imaging system will be of lower quality (less sharp) than the original measured subject, therefore $M > \hat{M}_I$ and consequently $MTF_I < 1$.

In this section, the visual perception of an optically captured or tomographically reconstructed image has been linked to the spatial frequency components of the image, thus enabling objective quantification of the spatial resolution.

F. MTF thresholding

A complex image will contain a spectrum of spatial frequencies *f*. The MTF can be computed using equation (2). The plot of the amplitude of the MTF will have similar form to fig. 2.

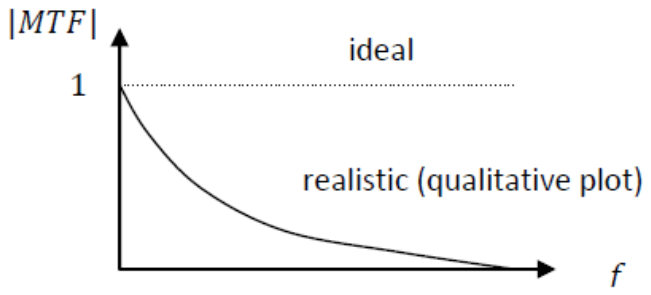

FIG. 2. Amplitude of the *MTF* versus spatial frequency at a single point in a complex image for an ideal (dotted line) and realistic (solid curve) imaging system.

The amplitude, which also depends on the initial intensity modulation depth, is typically normalised at zero spatial frequency (mean intensity). It can be observed that the imaging system acts as a low-pass filter on the spatial frequency content of the imaged subject.

The amplitude can remain non-trivial even at high spatial frequency components. A cut-off spatial frequency f_c is defined, above which the intensity amplitude of the spatial frequency components is insufficient for detection. The behaviour of the threshold at the cut-off point is that of a brick-wall low-pass filter.

The spatial frequency cut-off could be varied for different studies, but doing so would defeat the objectivity of this method. Therefore, a threshold is arbitrarily set. Providing that the cut-off point is standardised, qualitative objectivity is maintained and direct performance comparison studies can be made between, e.g. imaging array design iterations in tomographic imaging systems. A cut-off point at 10% of the maximum amplitude of MTF is recommended, as it is widely adopted[4,5,33] and appropriate for an interpretation stage implemented as a monitor and observer. For stricter quantification a cut-off at 20% can be adopted. Additional work on precisely defining the cut-off for a given application would further improve the quantitative accuracy of the subsequent spatial resolution measurements.

G. Translating to the spatial domain

The cut-off frequency can be related back to the spatial domain by the Rayleigh criterion as applied to the 2-D PSFs of two point distributions. The Rayleigh criterion describes a diffraction-limited optical imaging system, however the resolution criterion for two closely spaced PSFs remains applicable to a tomographic imaging system. If the PSFs of spatial width equal to half the spatial period *T* (spatial frequency expressed in

line-pairs per unit length) are separated by a linear distance q, then the PSFs will remain resolvable if $q>T/2$ (see fig. 3). The spatial width becomes the limiting spatial resolution δ_x by setting $T=1/f_c$, as described by equation 8:

$$\delta_x \approx \frac{1}{2f_c} \tag{8}$$

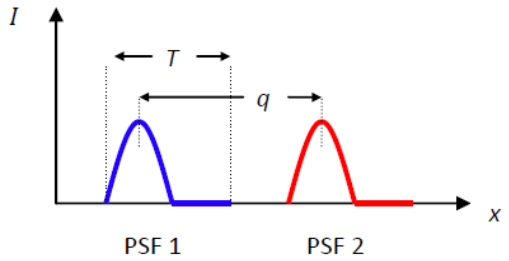

FIG. 3. PSFs of spatial period T are brought ever closer by decreasing linear separation q.

The Rayleigh criterion, or FWHM figure for this matter, could be applied directly instead of considering the spectral content of the PSF using the MTF. However, this can lead to gross inaccuracy if the shape of the derived PSF profile deviates significantly from a 'bell-shaped' curve such as an Airy disk or a Gaussian distribution.

This scenario is exemplified by the experimental data obtained when the method was applied to the CST system used in this work. In figure 13 a plateau is observed on the left-hand side, at the beginning of the intensity rise width. The plateau is then mirrored to the right hand side. The scenario is exaggerated and presented in fig. 4.

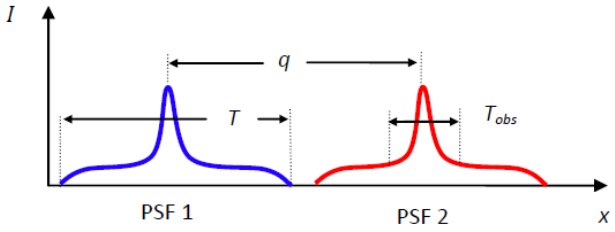

FIG. 4. Scenario where the profile of the PSFs substantially deviates from a 'bell-shaped' curve.

If the Rayleigh criterion for limiting spatial resolution were to be applied directly to this intensity profile then the limiting spatial resolution would occur when $T=q$. However, an observer is likely to perceive the spatially extended low-level intensity as a 'background' to the feature and focus on the peak instead. In this case the spatial periodicity of the feature would be more accurately described by T_{obs}. Consequently, $\delta_{x\_obs} < \delta_x$, which is incorrect. A similar argument can be made for the FWHM figure if the plateau described was to exist after the half-maximum point on the intensity curve.

The shape of the intensity profile curve cannot be overlooked when evaluating the limiting spatial resolution, as figures based on single-point criteria (Rayleigh and FWHM) can in this case be inaccurate. In this respect the new method described here considers the entire shape of the curve and then creates synthetic, yet equivalent, Airy disks to determine the limiting spatial resolution from.

H. Conception of a practical test phantom

The spatial resolution quantification method requires the PSF of the imaging system to be determined. Such a measurement is impractical as an ideal point source is difficult to produce and when placed in a sparsely-sampled imaging space it will likely not overlap with a sufficient number of measurement beams for tomographic reconstruction.

An alternative way of imaging a point is by approximating a line as an infinite number of points (see fig. 5). The imaging system response in the form of the reconstructed line is then the LSF. Given the LSF, the PSF can be estimated by taking a slice perpendicular to the LSF at any desired position. It must be noted that only the intensity information perpendicular to the LSF is valid, as for any other direction the intensity is superimposed with that of the neighbouring PSF. However, a 360° PSF can be reconstructed if angular symmetry is assumed. This assumption is justified since the PSF will be much smaller in size compared to the imaging space and spatial resolution capability of the imaging system.

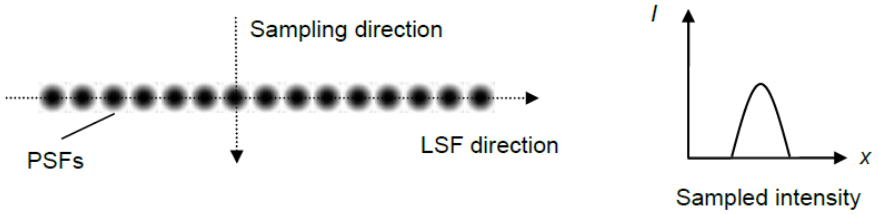

FIG. 5. LSF approximation by a series of PSFs (left) and intensity profile along sampling direction (right).

A fine line feature remains difficult to fabricate in a practical phantom, so the thickness of the line is increased to the point where the line becomes a rectangle. The reconstruction of the edges of the rectangle yields the ESF. The LSF can be estimated from the ESF by differentiation with respect to the sampling direction which is perpendicular to the edge[34]. Similarly to the estimation of the PSF from the LSF, estimation of LSF from the ESF only provides valid information for one side of the LSF. Once again, symmetry can be assumed.

The above process is described by equations (9) and (10) for a point on the LSF at position y_0 as follows:

$$\frac{d}{dx}ESF(x,y)=LSF(x,y)\xrightarrow{y=y_0}LSF(x,y_0)=\left|PSF(x,y_0)\right| \tag{9}$$

Then computing the MTF at position y_0:

$$\left|DFT\left(PSF\left(x,y_0\right)\right)\right| = \left|MTF_{y0}\left(f\right)\right| \tag{10}$$

To summarise, a spatial resolution quantification phantom will contain a feature with at least one sampling edge (e.g. a rectangle). The feature is created using materials suitable for the imaging modality. Provided that the concentration is within a range that doesn't hinder tomographic reconstruction, its precise value is not significant as the MTF is normalised. However, the steepness of the concentration gradient must approximate that of a 'step input' to adequately stimulate the imaging system.

I. Imaging space segmentation

The quantification method described thus far can be applied to an infinitesimal area of the imaging space and produce an exceedingly detailed map of spatial resolution, limited only by the phantom's positioning accuracy and resolution. However, the penalty incurred by a large number of measurements and subsequent image reconstructions should be weighed against the spatial resolution the system can realistically achieve. A large number of measurements and a highly-detailed spatial resolution map should be reserved for systems with comparable spatial resolution performance.

To balance the number of required measurements against the expected spatial resolution performance, the imaging space is divided, or segmented, into conceptual areas (hereby called Sectors), within which the spatial resolution is assumed to be uniform and finite. A single measurement and image reconstruction falling within the Sector is then sufficient to determine the spatial resolution in that area. It is stressed that the segmentation is purely conceptual; no object is placed in the imaging space (see section IV.A. for the segmented imaging space in this work).

The Sectors are rectangular, of width W and length M. This shape facilitates averaging of the ESF, as explained later. Choosing smaller dimensions in an application will result in a more detailed spatial resolution map, albeit a more arduous data collection process. The width of each Sector must be set to the predicted spatial resolution if a model is available, or alternatively to a realistic estimate plus 30% margin. Doing so allows the full rise-width of the intensity to be captured, as well as providing isolation between adjacent intensity profiles as the sharp-edge is moved to the next Sector. The length M is selected arbitrarily.

The sharp-edge is positioned so that it coincides with the middle of a Sector at $W/2$ and tomographically reconstructed. In the reconstructed image, the spatially-varying ESF enclosed by the Sector is averaged along the M dimension, viz. along the length of the sharp-edge enclosed by the Sector. The averaged ESF is analysed

as described previously. Then, the sharp edge is translated to the next Sector and the process repeated for all Sectors.

The rectangular Sectors can occupy the entirety of a rectangular imaging space, thus fully sampling it. However, for a circular imaging space, regions between Sectors will remain un-sampled. These, albeit being small, can be sampled by redistributing the rectangular Sectors inside the imaging space.

III. EXPERIMENTAL APPARATUS

The spatial resolution quantification method described in section 2 was applied to a CST system utilising the Near-IR Absorption Tomography (NIRAT) modality. The method can be applied using results obtained by simulation of the test concentration or by experimentally creating the test concentration. We opted for an experimental approach to encompass the effect of measurement noise thus more closely emulate the CST system in its final application.

A. Background applications

Chemical Species Tomography offers an attractive means of visualising the spatial distribution of chemical species (e.g. CO, CH_4, H_2O, etc.) that are of interest in numerous industrial applications. The technique is minimally-intrusive and can image the distribution at typically 100k frames/s without having moving parts. Particularly the NIRAT modality has been previously employed for Hydrocarbon (HC) concentration distribution imaging[9,35] in the combustion cylinder of a Spark-Ignition (SI) engine. The same instrumetation system was used, with different wavelengths, for demonstration of H_2O spectroscopy[36] measurements. The system described herein was later employed for in-cylinder HC concentration distribution imaging in a Compression-Ignition (CI) engine. These applications are characterised by relaxed spatial resolution requirements but, due to the processes involved, demand fast sampling.

B. Spectroscopy & Dual-Wavelength Ratiometric (DWR) Measurements

In the case of HC imaging, NIRAT exploits the spectrally wide and relatively unstructured spectroscopic absorption feature that all partially or fully saturated hydrocarbons display at 1700nm[37]. In order to suppress non species-specific phenomena, a reference wavelength is typically introduced which demonstrates negligible spectroscopic absorption by all other species present in the imaging space[38]. In general, the spectral separation of the measurement and reference wavelengths is kept small so as to avoid measurement errors due to chromatic dispersion effects.

C. Instrumentation functional description

The instrumentation system, whose architecture has been described more fully in[38], consists of (see fig. 6) two LASER sources at 1700nm (λ_{meas}) and 1651nm (λ_{ref}), modulated at 300kHz and 500kHz respectively. The source at 1651nm is used as the reference wavelength. The resulting spectral separation of 49nm, compounded with the data conditioning algorithm described herein, averted the introduction of significant chromatic dispersion errors in the measurements[39]. The two sources were combined into a single-mode optical fibre using Wavelength-Division Multiplexing (WDM) and then divided into 31 beams which were subsequently guided to and from an optical access plate by means of further optical fibres. On the optical access plate, the beams were collimated and launched into the imaging space forming a co-planar grid -the beam array- arranged in 4 projections of equal angular separation and consisting of 10-5-10-6 beams respectively. The imaging space of interest is circular and has a diameter of 81mm as defined by an optical access ring as used on the CI engine (see fig. 6). As the entirety of the imaging space is covered by the tomography system, the dimension of the imaging space can be considered to be the Field Of View (FOV) of the tomography system in this paper.

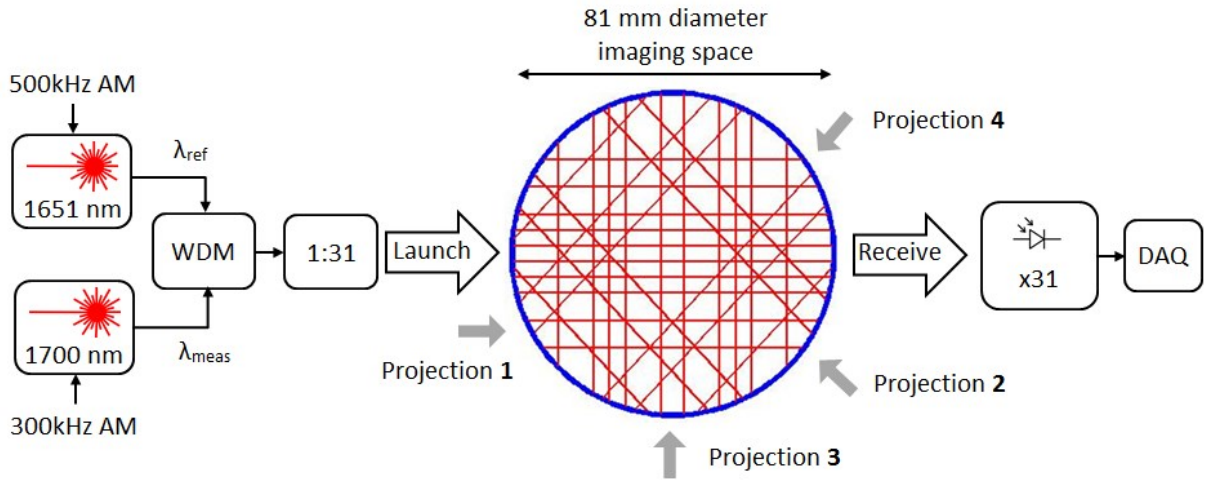

FIG. 6. Schematic diagram of the instrumentation. The optoelectronic systems, imaging space and tomographic imaging array consisting of 31beams are shown.

The beams traverse the imaging space of interest which contains an unknown, spatially-varying, HC distribution. Consequently, the measurement wavelength experiences spectroscopic absorption according to the Beer-Lambert law. The optical intensity of the collected beams was measured using photodiodes and the signal from each wavelength was demodulated before being digitised.

D. Choice, justification and spectroscopy of propane

The phantom developed employs a free-space flow of non-combusting, technical grade, gaseous propane (C_3H_8) as the target species. Propane consists of a single chain of C-C and C-H bonds and as such demonstrates

spectroscopic behaviour that qualitatively (shape and spectral location of absorption features) mimics general hydrocarbons, including the C8 and C12 hydrocarbon-based fuels that the CST system was designed to target.

The absorption coefficients of propane at the wavelengths, temperature and pressure involved in this experiment have been previously reported[40]. In this work an absorption coefficient of 77 litres*mol-1*m-1 was adopted as it was estimated[38] under near-identical conditions to the ones present in the measurement space of the gaseous phantom apparatus.

Propane was chosen over other media due to three other considerations. Firstly, a medium in low density gaseous phase was used in order not to introduce excessive spectroscopic absorption of the beams traversing the medium, thereby allowing detection of the transmission signal. Secondly, the gas delivery equipment was already available from previous experiments in the Group[12]. Thirdly, other simple alkanes such as methane, ethane and butane were considered but rejected due to safety concerns arising from their density relative to air or the need for equipment recalibration[39].

E. Nitrogen co-flow

The flow of propane inevitably entrains surrounding air. The process of entrainment introduces turbulence near the edge of the flow. The turbulence creates small-scale discontinuities in the optical characteristics of the medium that randomly modulate the coupling of the launch and receive optics and ultimately have an adverse effect on the SNR of the absorption signal[39]. To suppress this phenomenon a co-flow of technical-grade nitrogen (N_2) was introduced. Nitrogen was selected as it mimics ambient air while not demonstrating spectroscopic absorption at the wavelengths employed. The flow velocities of the propane and nitrogen flows were matched based on their relative cross-sectional profiles. In circular-plume experiments using this setup[39] the introduction of a co-flow was shown to substantially improve the SNR of the measurements.

F. Flow-conditioning nozzles

A quasi-rectangular nozzle (see fig. 7) was used to create the sharp-edged feature required by the spatial resolution quantification method. The precise cross-sectional geometry of the nozzle is a trapezoid in order to avoid disturbance of the flow from the optical access ring. The resulting cross-sectional profile of the propane flow is 10mm wide and its length matches the diameter of the optical access ring, i.e. 81mm. The nitrogen co-flow was introduced using an identically-sized nozzle placed adjacent to the propane nozzle. The separator was retracted by 5mm from the exit orifice and flared to a sharp edge, thereby allowing the gases to come in contact prior to exiting the nozzle. At the gas entry side of each nozzle a plenum chamber and sintered diffuser were used to create a laminar flow. To further aid this process, the length of both nozzles was made equal to 3x the width i.e. 30mm.

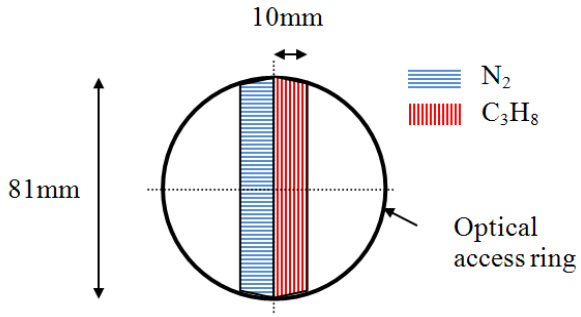

FIG. 7. Cross-sectional profile of gas delivery nozzle.

G. Gas supply & collection

For the propane supply, a standard 5kg cylinder was used and for the nitrogen supply, a 'K' size cylinder was used and regulators limited the supply pressure to 1.5bar and 2.0bar respectively. The propane line was fitted with a flashback arrestor. Flow-meters were used to set the desired flow rate. The temperature of both gas supplies was returned to ambient prior to reaching the nozzle using a simple water-filled heat exchanger. The gas supply system is shown in figure 8.

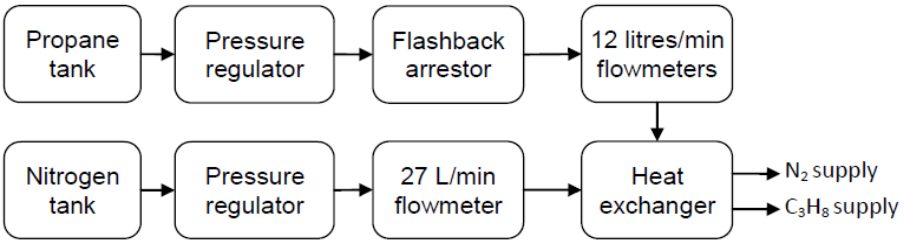

FIG. 8. Schematic representation of the gas delivery system.

After the gases had travelled through the optical access ring, they were collected in a 47 litre steel container. Following an experimental session, the container was transferred to a fume hood where the mixture was

dissipated at a safe rate. Ten 1mm diameter holes at the bottom of the vessel (closed during the experiment) facilitated the purging process.

H. Safety measures

Numerous safety measures were put in place. The maximum fill time and fume hood venting rate were calculated to ensure the mixture strength remained below the Lower Explosive Limit (LEL) of propane. The air surrounding the experiment was monitored for combustible gases, ignition-free zones were enforced and an equipotential scheme was introduced to limit the risk of electrical discharge. Finally, required risk assessments were conducted and iterated, as was the experimental set-up, to reach a safe procedure. The entire experimental setup is shown in fig. 9.

I. Experimental validation of plume's sharp edge

Shadowgraphy was used to ascertain that the transition between the nitrogen and propane flows was sufficiently steep for the edge of the test plume to be considered 'sharp', as dictated by the spatial resolution quantification method. The experimental apparatus, designed after[41], has previously been described in detail[39]. The experiment showed that the linear width of the nitrogen-propane flow boundary crossing at the level of the imaging plane was ≈1.4mm. This figure is substantially lower than the expected spatial resolution of the system as estimated by equation (1). Consequently, the test plume can be considered to be 'sharp-edged'.

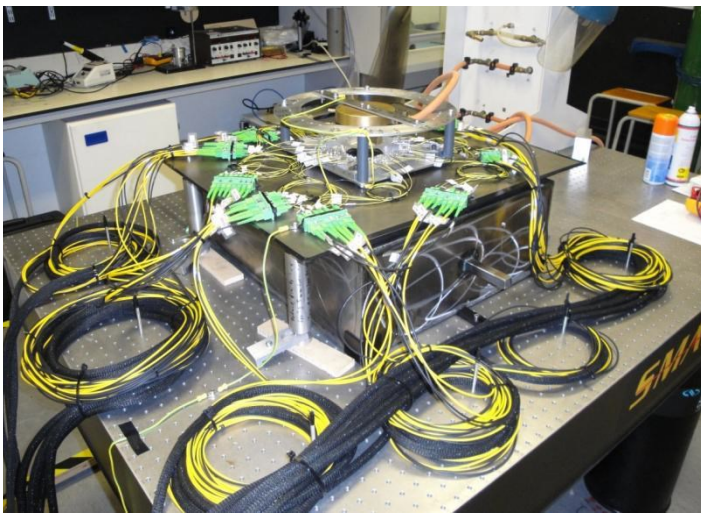

FIG. 9. Complete gaseous phantom experimental setup with CST system installed.

IV. METHOD APPLICATION

A. Segmentation of imaging space & nozzle translation scheme

The disk-shaped imaging space of the CST system was segmented into rectangular Sectors arranged in radial Tracks (see fig. 10). Each Sector is of radial length *M* and width *W*. To define the Sectors' dimensions, an

approximation of the system's spatial resolution was calculated using equation (1) for m=31 and D=81mm. For these values, δ_x=14.54mm (≈D/5). From experimental results in previous works[12,39], the spatial resolution is better (smaller) than that predicted. Therefore, no margin was added and the Sectors' width W was set to 15mm. The Sectors' radial length M was arbitrarily set to 10mm. A total of 28 Sectors were fitted inside the imaging space in 4 Tracks and uniformly distributed. The two Sectors in the central Track have a radial length M of 5mm. This was a compromise between having Sectors of different radial length and leaving a large area in the centre not sampled. In total, 16 different nozzle angular positions (see table I) were required for data to be acquired for all Sectors. To facilitate locating of the nozzle at the desired angular positions, the nozzle was mounted on a bar (see fig. 11) which was in turn supported on a ring with locating holes at the desired positions.

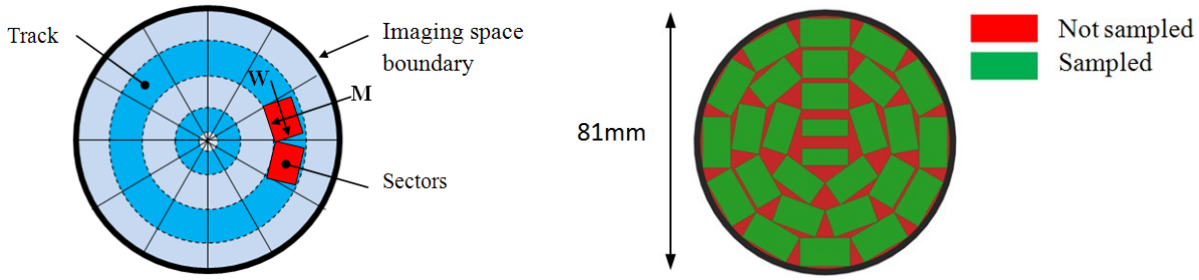

FIG. 10. (Left) A circular imaging space is segmented into concentric Tracks containing rectangular Sectors. (Right) The imaging space in this work is segmented in 28 Sectors in 4 Tracks.

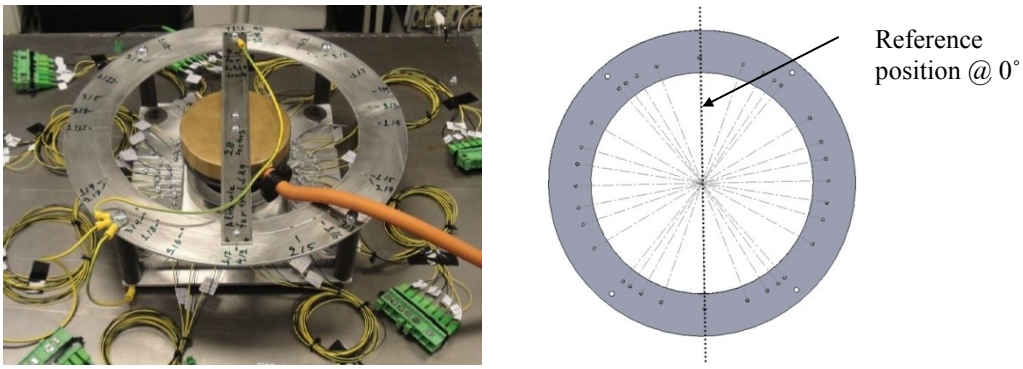

FIG. 11. (Left) Angular translation scheme for gas nozzle. (Right) The 16 angular positions used in this work.

Table I. Nozzle angular locations used in this work for sampling all the Sectors in all the Tracks.

		Sector #											
		1	**2**	**3**	**4**	**5**	**6**	**7**	**8**	**9**	**10**	**11**	**12**
Track #	**1**	0°	30°	60°	90°	120°	150°	0°	216°	60°	90°	120°	150°
	2	0°	40°	80°	120°	160°	200°	60°	280°	320°			
	3	0°	72°	144°	216°	288°							
	4	0°	0°										

B. Raw data acquisition

The raw data simultaneously acquired at 100kS/s comprises the received optical intensities of the measurement and reference wavelengths for all the beams in the array. In the first experimental phase, raw data was acquired for 5s with the LASER sources ON but without any gas flow, thereby establishing the maximum intensities (hereby 'full-scale, FS'). The LASER sources were then switched OFF and the (internally generated) static offsets present in the raw data (hereby 'offset, OS') were recorded for 5s. In the second experimental phase, the flow rate of both gases was set to 6litres/min, at 289.3±0.8K and 1040±1mbar. The nozzle was translated at each angular position and raw data (hereby 'gas-flow data') was acquired for 10s.

C. Raw data conditioning

The extracted raw data was conditioned (see equation 11) prior to image reconstruction. To ensure the gas flow was stable, only raw data acquired between the 5th and 6th acquisition second (middle of acquisition period) was extracted for further conditioning. The raw data conditioning algorithm begins by computing the mean of the OS and FS measurements. The gas-flow data as well as the FS are offset-corrected by subtraction of the mean of the offsets. The offset-corrected gas-flow data was then normalised to the dynamic range. The offset-corrected and normalised gas-flow data was then averaged over the whole 1s period. Finally, the intensity ratio of the measurement to the reference wavelengths was computed, to obtain the DWR data for image reconstruction.

$$DWR = \frac{\left(\frac{I_{\lambda meas} - \bar{I}_{\lambda meas_{OS}}}{\bar{I}_{\lambda meas_{FS}} - \bar{I}_{\lambda meas_{OS}}} \right)}{\left(\frac{I_{\lambda ref} - \bar{I}_{\lambda ref_{OS}}}{\bar{I}_{\lambda ref_{FS}} - \bar{I}_{\lambda ref_{OS}}} \right)} \tag{11}$$

D. Image reconstruction

Image reconstruction was performed using the iterative Landweber method[12], using 25 iterations and a relaxation coefficient of 0.00354. To regularise the solution, a median filter of size 5x5 pixels was applied to the reconstructed image domain within each iteration. These parameters have previously been optimised for imaging of circular test plumes[39]. The propane concentration for the initial solution to the forward problem was set to 0.042±0.0001mol*litre-1 and the absorption co-efficient to 77 litres*mol-1*m-1. The pixel intensity in the reconstructed images was globally normalised across all images. The dataset of reconstructed images can be seen in figure 15.

E. Inter-Sector intensity profile averaging

The segmentation pattern described earlier was superimposed on the imaging space to isolate each Sector. Here we arbitrarily selected Sector #2 from Track #2 (see fig. 12a, captured with the nozzle positioned at 40°). The intensity of the pixels enclosed by the Sector's profile is shown in fig. 12b. A total of 12 pixel vectors were created for this Sector, perpendicular to the sharp-edged nozzle profile. The pixel intensity along the first and last vectors (1 and 12) is shown for illustration. The remainder of the process was repeated for all Sectors in all Tracks to produce the spatial resolution map of the system as shown in figure 16.

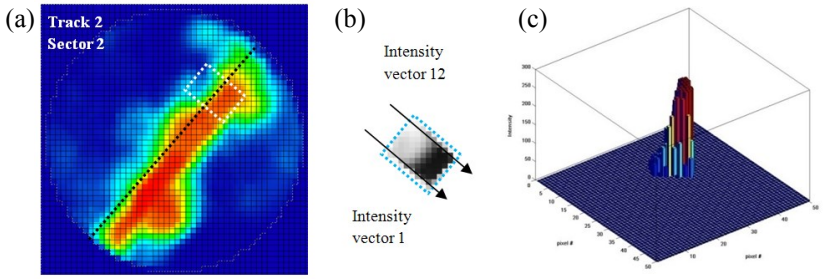

FIG. 12. (a) Area enclosed by Sector 2 on Track 2, (b) isolated intensity profile with intensity vectors and (c) 3D intensity plot of Sector 2 on Track 2 isolated in the imaging space.

The individual intensity vectors were averaged to produce the ESF for this Sector (see fig. 13). Linear interpolation between the data points reduced the granularity of the plot.

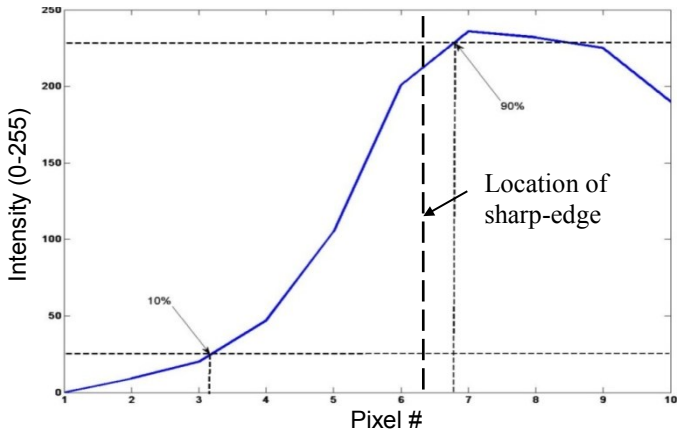

FIG. 13. Edge spread function for Sector 2 in Track 2 from its normalised intensity profiles.

F. Calculation of the LSF

The LSF was calculated by differentiating the ESF with respect to pixel number (step size = 1). The LSF was reconstructed using oversampling by a factor of 100 (see fig. 14). As the signal is essentially bandwidth limited, the normalised sinc(x) function was used for the interpolation. The left-half of the LSF was mirrored with respect to the intensity peak. This is justified by the assumption that the PSF is circularly symmetrical and therefore the LSF, being a slice of the PSF, must also be symmetrical. This condition would occur naturally in

an ideal tomographic imaging system and absorption target. Here, the assumption is valid when the reconstruction analysed is 'representative enough' of an edge, as expected for a tomography system with severely-limited views.

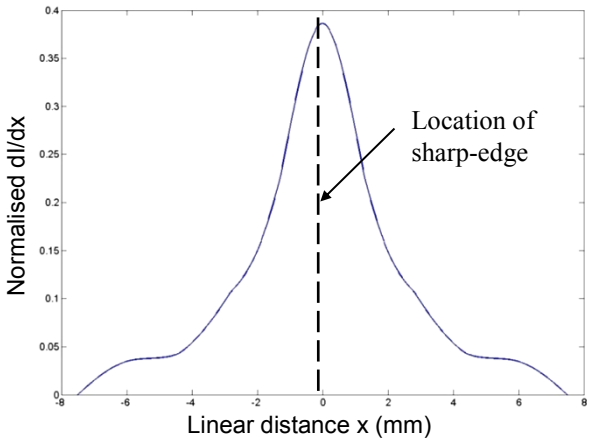

FIG. 14. LSF calculated by differentiating the ESF in figure 12.

G. Calculation of the MTF and thresholding

The MTF was calculated by taking the 2-D DFT of the LSF. The modulation intensity threshold was set to 20% of the maximum, corresponding to a highest pass spatial frequency of ≈0.05 line-pairs/mm (see fig. 15). Using equation (8), the spatial resolution for this Sector is 10mm. The results for all Sectors are tabulated in table II.

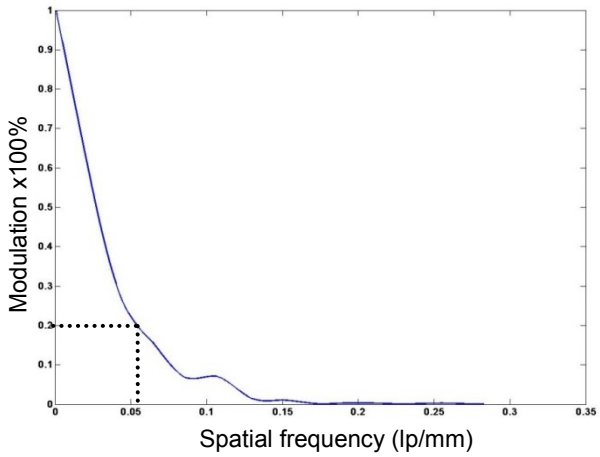

FIG. 15. Modulation transfer function for Sector 2 on Track 2. The 20% intensity threshold is shown.

V. RESULTS

The nozzle was translated at each angular position outlined in table I and data acquired. The reconstructed images are presented in figure 16 below. The diameter of the imaging space, i.e. FOV, is 81mm.

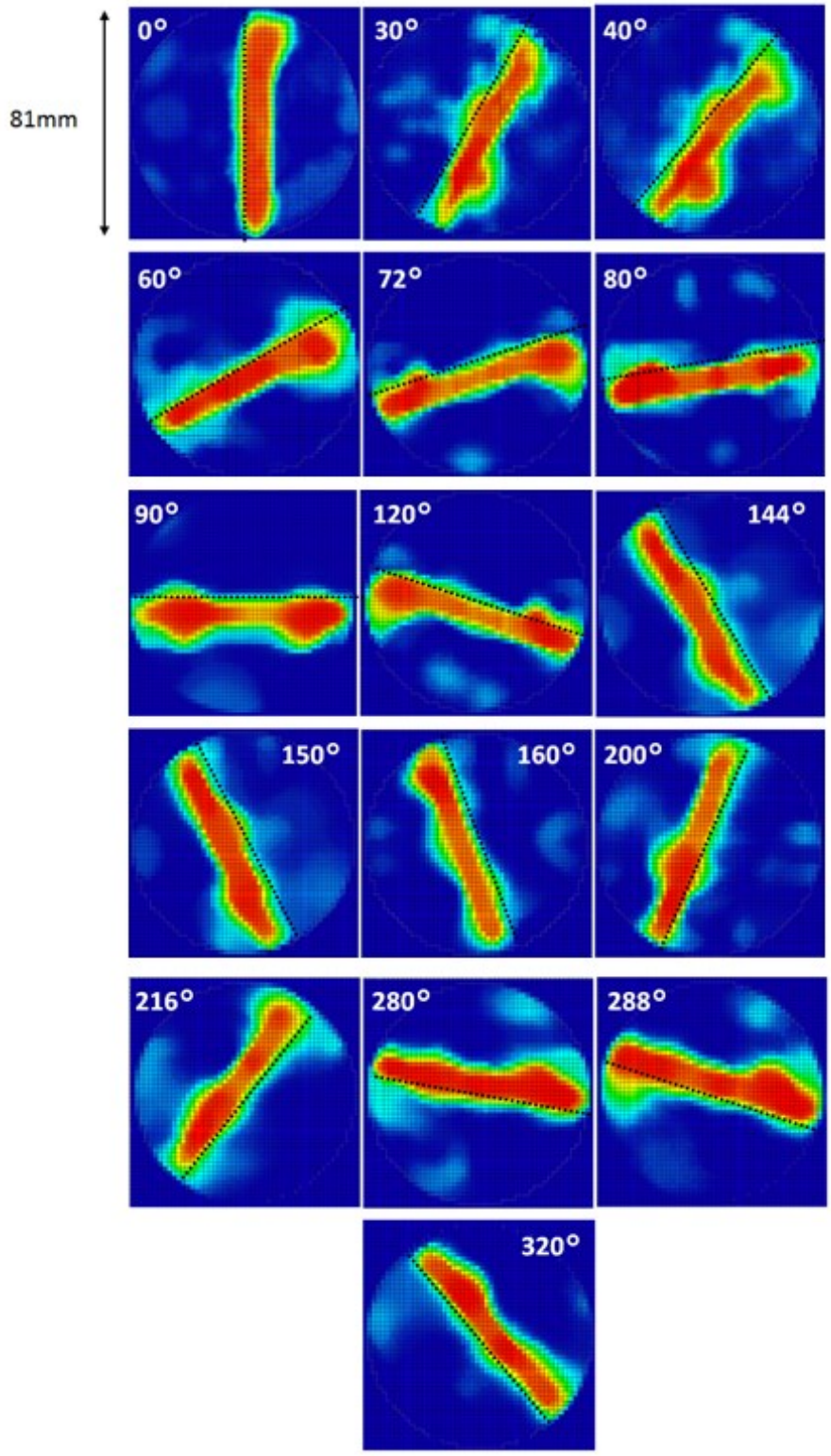

FIG. 16. Reconstructions of the rectangular sharp-edged feature at all angular positions.

The limiting spatial resolution for all sectors and all tracks is tabulated in table II and the spatially-resolved limiting spatial resolution is presented in figure 17.

Table II. Limiting spatial resolution (in mm) in all Sectors of the imaging space.

		Sector											
		1	**2**	**3**	**4**	**5**	**6**	**7**	**8**	**9**	**10**	**11**	**12**
Track	**1**	8	14	12	7	9	8	7	13	13	8	7	11
	2	4	10	7	8	13	5	13	7	8			
	3	5	8	10	8	10							
	4	6	6										

Mean = 9 mm

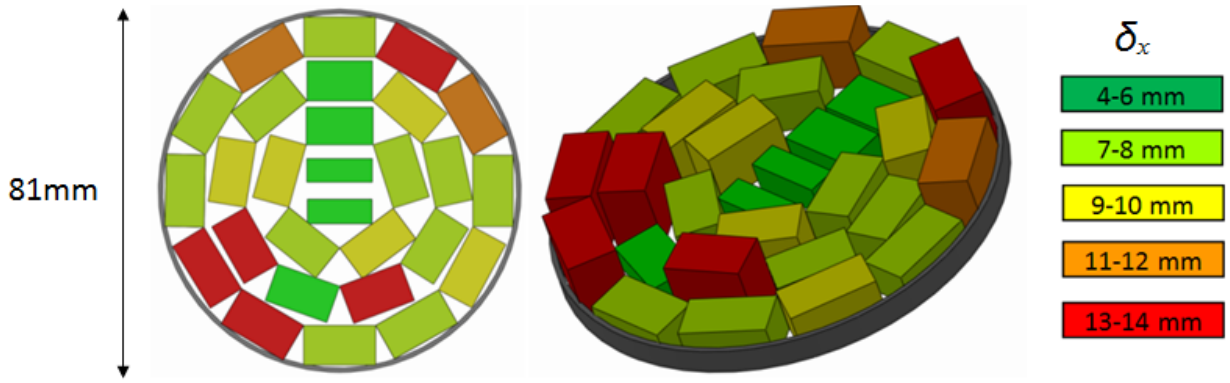

FIG. 17. Map of the limiting spatial resolution of the holistic tomography system.

VI. DISCUSSION

A. Numerical results in brief

The results indicate that the spatial resolution significantly varies as a function of position within the imaging space by about 60% of the mean. Approximately half of the number of Sectors (11 out of 28) achieve a spatial resolution between 7 and 8mm. The average spatial resolution across the entire imaging space is 9mm (equivalent to $D/9$). The best (smallest) spatial resolution achieved is 4mm and the worst (largest) is 14mm.

B. Comparison with previous results

The best spatial resolution figure of 4mm ($D/20$) achieved in one Sector is 363% better than theoretically estimated[19] and 405% better than anticipated from previous experiments[42]. In the latter study a regular beam array of 32 beams was used (4 projections, 8 beams each). In a more recent study[12] using an irregular array of 27 beams, a numerical figure for spatial resolution is not stated, however the image reconstructions imply a spatial resolution of ≈7mm ($D/12$) in specific regions of the imaging space (see fig. 13d, in[12]).

C. Spatial resolution distribution and symmetry

Examining the distribution of the spatial resolution performance, the best performance is achieved in Sector 1 of Tracks 2, 3 and 4 (see fig. 15). These Sectors are collinear (y-y' axis) and were sampled with the test flow positioned at 0° i.e. vertically. Sectors 1 and 7 of Track 1, demonstrate identical performance to each other yet worse performance than the Sectors nearer to the centre, albeit resting on the same line and sampled simultaneously.

The worst performance is demonstrated at the bottom left of the imaging space, Sectors 8 and 9 of Track 1 and Sectors 5 and 7 of Track 2. Very good performance is achieved in Sector 6 of Track 2, despite it being surrounded by poor spatial resolution Sectors.

Observations regarding the symmetry of the spatial resolution performance could be hazarded, especially when symmetry is intuitively expected given an axi-symmetrical beam arrangement. However, the lack of consistent (axi-symmetric) and widespread (2 or more Sectors) symmetry in the results would make such an assertion unfounded.

D. Proposed mechanism for observed behaviour

The mechanism proposed to explain the aforementioned spatial resolution map observations is based on the correlation between the positions of the test concentration and sampling beams in the presence of measurement noise and reconstruction algorithm-induced spatial filtering.

The image reconstruction algorithm, as described earlier, applies a median filter to the reconstructed image domain within each iteration. The side-effect of the spatial filtering is smoothing of sharp edges present in the reconstruction. The presence of beams in close proximity, ones that do not interact with the flow, counteract the edge smoothing by effectively 'bounding' the reconstructed distribution, resulting in locally better defined edges and improved spatial resolution. Such beams will be termed 'bounding beams' due to their effect.

The vertical and horizontal projections (0° and 90°) consist of a relatively large number of closely spaced beams, whereas the cross projections (45° and 135°) consist of fewer, more sparsely spaced beams. When the test concentration is positioned at 0° or 90°, the spacing between the edge of the flow (flow boundary) and adjacent beams (hereby beam-flow spacing) is ≈1.6mm. In contrast, at 45° and 135° the beam-flow spacing is ≈7.7mm. Despite their close proximity, the beams do not interact with the flow (as confirmed by shadowgraphy and the raw data) and therefore experience no spectroscopic absorption. Consequently, the effect of the bounding beams when the test concentration is located at 0° is exaggerated and the corresponding Sectors demonstrate the best spatial resolution performance. The somewhat poorer performance of Sectors 1, 7 of Track

1 can be attributed to measurement noise introduced by the increasingly turbulent flow near the corners of the rectangular flow. This suggests that Sectors 4 and 10 of Track 1 that are sampled when the test flow is located at 90° (horizontal) should demonstrate similar performance and indeed this is the case.

E. Beam array design guidelines and independent work

It is thereby submitted that, when no spatial information about the concentration can be provided or assumed, a regular beam array (i.e. one whose sampling points extend equally in the linear and angular axis of the sinogram space) is preferred over an irregular array in the sense that the sampling deficiency is uniformly distributed across the imaging space.

However, a regular beam array using a fixed number of beams and covering the entire imaging space implies that, in order to maintain the maximum localised beam density otherwise achievable by an irregular array, a higher number of beams is needed.

Other studies using different approaches also concluded that a regular beam array is preferred. Firstly, a general improvement of the image reconstructions of circular gaseous plumes was observed when a transition was heuristically made to a more regular beam array[12]. However, due to physical constraints the total number of beams was reduced from 32 to 27 in order to increase the number of projections.

Secondly, parametric sweeps (e.g. beam spacing) on generic 126-beam array geometries were performed[43] in order to minimise the discrepancy between a test distribution and its reconstruction. The discrepancy was minimised when a regular beam array was used.

With regards to the practical implementation of a regular array, it has been shown[18,44] that the optimum distribution of sampling points in the sinogram space is that of a 120°-sided honeycomb or rhombic lattice. The implication of this approach is that the number of sampling points per unit area is minimised, whereas in the Cartesian space the number of beams per projection is equal to the number of projections.

F. Implications of the superposition assumption

Accurate results are produced when analysing the reconstruction of a sharp edge within a Sector. The test feature's profile outside the Sector is not part of the analysis, thus the profile of the test feature does not need to be rectangular. For example, the arc of a circular test feature enclosed within a Sector can approximate a straight sharp edge if the test feature has sufficiently large diameter.

However, in practice, the intensity profile within a Sector is partly influenced by the profile and magnitude of the concentration in the remainder of the imaging space, i.e. superposition applies only partly. This limitation however arises from the severely under-sampled imaging space and not the quantification method per se.

To maintain objectivity it is recommended that the profile and concentration of the test feature are controlled when multiple array designs are tested.

VII. CONCLUSIONS

A. Overview

We have described a method for the systematic quantification of limiting spatial resolution of a tomography system. Treating the entire tomography system as a 'black-box' ultimately allowed the bottom-line spatial resolution performance to be realistically evaluated. Having based the quantification method on the analysis of the spatial frequency content of the reconstructed images eliminated the need for an observer to judge the spatial resolution, thus making the method objective and readily standardised.

B. Practical phantom

The intrinsic difficulty associated with the use of the PSF is the introduction of a point source in a sparsely sampled imaging space. To overcome this, the PSF was approximated indirectly, beginning with the ESF and then computing the LSF which was sampled at the desired location. By allowing the test profile to have non-zero dimensions on both axes, the design of a practical, sharp-edged test phantom became feasible.

C. Imaging space segmentation

The spatially-varying attribute of the spatial resolution performance was addressed by segmenting the imaging space into a number of Sectors and evaluating the performance within each Sector. The selected rectangular shape of the Sectors facilitated subsequent analysis but resulted in areas of the circular imaging space remaining not sampled. The areas are substantially smaller than the Sectors, therefore no significant variation in spatial resolution performance is expected in the areas not sampled.

D. Experimental

The experimental application of the method using an established instrumentation system accurately captured noise sources that would typically require significant time investment to model in a simulation environment.

In implementing the experimental apparatus the difficulties of generating open-space flows of highly flammable gases were encountered. However, implementing careful experimental procedure and controls the risks were circumvented.

The creation of a laminar flow with a rectangular cross-section of high aspect ratio presented a particular challenge. The introduction of a chemically inert and spectroscopically silent co-flow agent significantly suppressed turbulence at the flow boundary. Nevertheless, using refractive index photography the behaviour at

the flow boundary was visualised to verify that the tomography system was indeed presented with a 'sharp edge'.

E. Image processing

The reconstructed images were analysed to arrive at the spatial resolution performance in each Sector. Occasionally in the image reconstructions low-intensity artefacts would span across multiple Sectors, preventing edge identification within the Sector. In these cases, treating the artefact as a background constant facilitated a solution that does not detract from objectivity.

The inherently small number of pixels per unit length in the reconstructed images resulted in a small number of data points to form the intensity profile plots. However, interpolation of the data points increased the number of samples thus allowing standard libraries in numerical computing packages to be used in calculating the Fourier Transform of the ESF.

Conclusions

In this paper we have presented a novel framework and experimental method for the objective and spatially-resolved quantification of the spatial resolution of a hard-field tomography system. The framework is not application-specific and therefore the experimental method can be adapted to other tomographic systems that potentially utilise a different modality. The framework presented is of significant utility in multiple occasions: 1) During the design phase, to optimise the spatial resolution in regions of particular interest or to select the optimum reconstruction algorithm, 2) During the verification phase to characterise the spatial resolution of the implemented system and 3) Following characterisation, to cross-compare the performance of multiple systems.

Acknowledgements

The authors acknowledge the financial and technical contributions received from the Engineering and Physical Sciences Research Council (EPSRC) and Shell Global Solutions UK.

VIII. APPENDICES

APPENDIX A: FLOWCHART OF METHOD

The flowchart summarises the stages of the spatial resolution method in this work and can be used as a guide when applying the method.

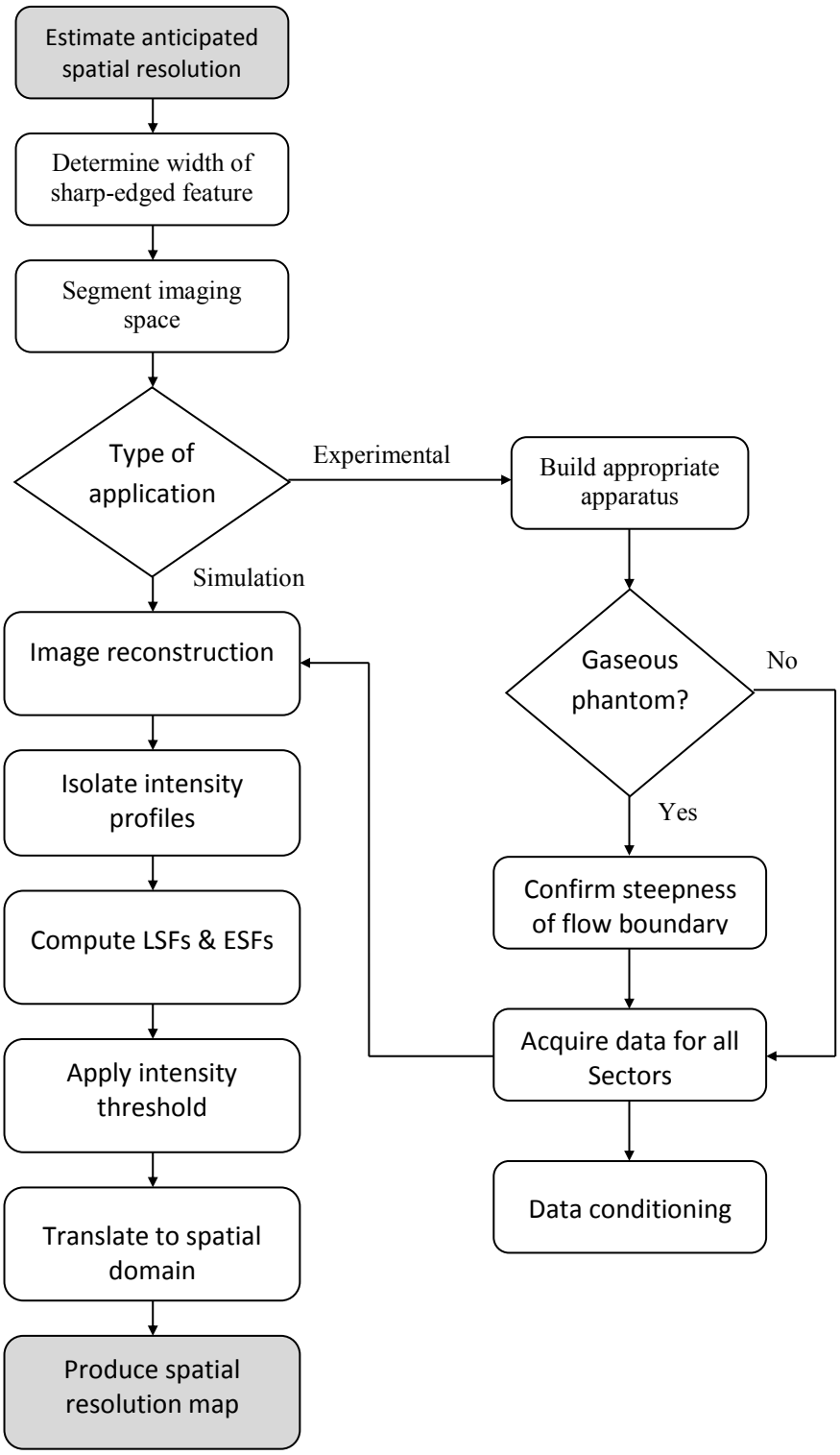

APPENDIX B: RIGOROUS CALCULATION OF THE MAXIMUM NUMBER OF SECTORS

The following is a rigorous method of determining the maximum number of rectangular Sectors that can fit in a circular space of a given diameter.

Let a rectangular Sector have radial length L and width W, inside an imaging space of radius R.

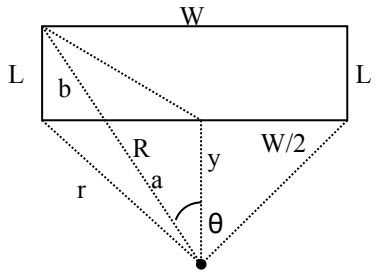

From Pythagorean theorem, $$r^2 = \frac{W^2}{4} + y^2$$ (Identity 1)

From the properties of similar triangles, $$\frac{y}{a} = \frac{L}{b} \Rightarrow b = \frac{La}{y}$$ (Identity 2)

From the drawing, $$a + b = R \xrightarrow{Identity2} a = \frac{Ry}{L+y}$$ (Identity 3)

From the cosine rule, $$L^2 + \frac{W^2}{4} = R^2 + Y^2 - 2Ry\cos\theta = R^2 + y^2 - 2Ry\frac{(L+y)y}{Ry}$$ (Identity 4)

Factorising identity 4 and solving for its root,

$$y^2 + \frac{W^2}{4} + L^2 - R^2 + 2Ly = 0 \rightarrow y = -L \pm \frac{\sqrt{4R^2W^2}}{2} = \frac{1}{2}\sqrt{4R^2 - W^2} - L$$ (Identity 5)

Simultaneously solving identity 1 and 5 for r we have, $$r = \sqrt{R^2 + L^2 - L\sqrt{4R^2W^2}}$$ (Identity 6)

Finally to find θ, $$\sin(2\theta) = \frac{W}{2r} \Rightarrow \theta = \sin^{-1}\left(\frac{W}{2r}\right)$$ (Identity 7)

The number of rectangles *s* that fit in a Track is then given by

$$s = floor\left(\frac{2\pi}{\theta}\right), \text{ for } R > \frac{\sqrt{L^2 + W^2}}{2}$$

$s = 0$ otherwise (Identity 8)

The process of computing the total number of rectangular Sectors that fit in the imaging space begins from the outer Track *k* using identities 5, 6, 7 and 8. Then, for the next Track *k+1*, set $R_{k+1} = y_k$ and repeat until the floor function returns 0 i.e. the tracks are too small for rectangular Sectors to fit. The total number of rectangular Sectors is the sum from all Tracks.

IX. REFERENCES

[1]Hecht, E. (2003). *Optics.* Addison-Wesley.

[2]Smith, W. J. (1966). *Modern Optical Engineering.* McGraw-Hill.

[3]Born, M. (1999). *Principles of Optics.* Cambridge: Cambridge University Press.

[4]Thurner, P., Beckmann, F., & Müller, B. (2004). An optimization procedure for spatial and density resolution in hard X-ray micro-computed tomography. *Nuclear Instruments and Methods in Physics , 225* (4), 599–603.

[5]Bonse, U., Busch, F., Günnewig, O., et al. (1994). 3D computed X-ray tomography of human cancellous bone at 8 microns spatial and 10 (-4) energy resolution. *Bone and Mineral , 25* (1), 25-38.

[6]Ballrick, W. J., Palomo, J., Ruch, E., et al. (2008). Image distortion and spatial resolution of a commercially available cone-beam computed tomography machine. *American Journal of Orthodontics and Dentofacial Orthopedics* , 573-582.

[7]Frieder, G., & Herman, G. T. (1971). Resolution in reconstruction objects from electron micrographs. *Journal of Theoretical Biology , 33* (1), 213-223.

[8]Scott, D., & McCann, H. (2005). *Process Imaging For Automatic Control.* CRC Press.

[9]Wright, P., Terzija, N., Davidson, J., et al. (2010). High-speed chemical species tomography in a multi-cylinder automotive engine. *Chemical Engineering Journal , 158* (1), 2-10.

[10]Graeme, G. (1995). *Photodiode Amplifiers: OP AMP Solutions.* McGraw Hill Professional.

[11]Tarantola, A., Zito, F., & Gerundini, P. (2003). PET instrumentation and reconstruction algorithms in whole-body applications. *Journal of Nuclear Medicine , 44*, 756-769.

[12]Terzija, N., Davidson, J., Garcia-Stewart, C., et al. (2008). Image optimization for chemical species tomography with an irregular and sparse beam array. *Measurement science and technology , 19* (9).

[13]Watson, A. (2013). A formula for the mean human optical modulation transfer function as a function of pupil size. *Journal of Vision , 13* (6).

[14]Campell, F., & Green, D. (1965). Optical and retinal factors affecting visual resolution. *Journal of Physiology , 181* (3), 576-593.

[15]Floyd, J., Geipel, P., & Kempf, A. M. (2011). Computed Tomography of Chemiluminescence (CTC): Instantaneous 3D measurements and Phantom studies of a turbulent opposed jet flame. *Combustion and Flame,158*(2), 376-391

[16]Pauwels, R., Beinsberger, J., Collaert, B., et al. (2010). Effective dose range for dental cone beam computed tomography scanners. *European Journal of Radiology , 81* (2), 267-271.

[17]Gillet, B., Hardalupas, Y., Kavounides, C., & Taylor, A. (2004). Infrared absorption for measurement of hydrocarbon concentration in fuel/air mixtures (MAST-B-LIQUID). *Applied Thermal Engineering , 24* (11-12), 1633-1653.

[18]Rattey, P. A., & Lindgren, A. (1981). Sampling the 2-D Radon Transform. *IEEE Transactions on Acoustics, Speech and Image Processing , 29* (5), 994-1002.

[19]Bertero, M. (1998). *Introduction to Inverse Problems in Imaging.* Taylor Francis.

[20]Natterer, F. (2001). Mathematical methods in image reconstruction. *Society for Industrial and Applied Mathematics*.

[21]Ishino, Y., & Ohiwa, N. (2005). Three-dimensional computerized tomographic reconstruction of instantaneous distribution of chemiluminescence of a turbulent premixed flame. *Japan Society of Mechanical Engineering In. J. Ser.B: Fluids Therm. Eng. , 48* (1), 34-40.

[22]Schwarz, A. (1996). Multi-tomographic flame analysis with a Schlieren apparatus. *Measurement Science and Technology , 7* (3), 406-413.

[23]Twynstra, M.G., & Daun K.J. (2012). Laser-absorption tomography beam arrangement optimization using resolution matrices. *Applied Optics* , 51 (29), 7059-7068.

[24]Prieto, E., Martí-Climent, J., Arbizu, J., et al. (2010). Evaluation of spatial resolution of a PET scanner through the simulation and experimental measurement of the recovery coefficient. *Computers in Biology and Medicine , 40* (1), 75-80.

[25]Nishikido, F. (2008). Spatial resolution evaluation with a pair of two four-layer DOI. *Nuclear Instruments and Methods in Physics Research , 584* (1), 212-218.

[26]Andersen, F., Klausen, T., Loft, A., et al. (2013). Clinical evaluation of PET image reconstruction using a spatial resolution model. *European Journal of Radiology , 82* (5), 862-869.

[27]Baechler, S., Kardjilov, N., Dierick, et al. (2002). New features in cold neutron radiography and tomography - Part 1: thinner scintillators and a neutron velocity selector to improve the spatial resolution. *Nuclear Instruments and Methods in Physics Research Section A: Accelerators, Spectrometers, Detectors and Associated Equipment , 491* (3), 481-491.

[28]Müller, B., Thurner, P., Beckmann, F., et al.(2002). Non-destructive three-dimensional evaluation of biocompatible materials by microtomography using synchrotron radiation. *SPIE - Developments in X-Ray Tomography III*, *178*, pp. 178-188. San Diego, CA.

[29]Gonzalez, R., & Woods, R. (2008). *Digital Image Processing* (3rd ed.). Prentice Hall.

[30]Goodman, J. (2005). *Introduction to Fourier Optics.* Roberts and Company Publishers.

[31]Efford, N. (2000). *Digital Image Processing: A Practical Introduction Using Java.* Addison Wesley.

[32]Russ, J. (2002). *Image Processing Techniques.* John Wiley & Sons, Inc.

[33]Lehmann, E. F., & Boillat, P. (2007). The micro-setup for neutron imaging: A major step forward to improve the spatial resolution. *Nuclear Instruments and Methods in Physics Research* , 389-386.

[34]Hols, G. (1998). *Sampling, aliasing, and data fidelity for electronic imaging systems, communications, and data acquisition.* JCD Publications.

[35]Cheadle, E., Karagiannopoulos, S., Terzija, N., et al. (2012). Fuel spray and vapour imaging in a single-cylinder research engine. *6th Int. Symp. on Process Tomography (ISPT-6).* Cape Town, South Africa.

[36]Karagiannopoulos, S., Cheadle, E., Wright, P., Tsekenis, S. A., & McCann, H. (2012). A flexible-wavelength scheme for low-noise gas measurements by Direct Absorption Spectroscopy. *Applied Optics , 51* (34), 8057-8067.

[37]Carey, S. (2001). *Chemical species tomography by near infrared absorption - Ph.D. dissertation.* University of Manchester Institute of Science and Technology.

[38]Wright, P., Garcia-Stewart, C., Carey, S., et al. (2005). Toward in-cylinder absorption tomography in a production engine. *Applied Optics , 44*, 6578-6592.

[39]Tsekenis, S.A. (2013). *High speed chemical species tomography for advanced fuels and engines - Eng.D. dissertation.* University of Manchester Institute of Science and Technology.

[40]Kjaergaard, H., Yu, H., Schattka, B., et al. (1993). Intensities in local mode overtone spectra: Propane. *The Journal of Chemical Physics , 93*.

[41]Settles, G. (1949). *Schlieren and Shadowgraphy techniques.* New york: Springer-Verlag Berlin Heidelberg.

[42]Hindle, F., Carey, J., Ozanyan, K., et al. (2001). Measurement of gaseous hydrocarbon distribution by a near infra-red absorption tomography system. *Journal of Electronic Imaging , 10*, 593-600.

[43]McCormick, D. Twynstra M.G., Daun K.J., & McCann H. (2013). Optimising laser absorption tomography beam arrays for imaging chemical species in gas turbine engine exhaust plumes. *Proc. 7th World Congress on Industrial Process Tomography (WCIPT-7)*. Krakow, Poland.

[44]Petersen, D.P. & Middleton D. (1962). Sampling and reconstruction of wave-number-limited functions in N-dimensional euclidean spaces. *Inf. Control,* 5 (4), 279-323

[45]Ruuskanen, A.R., Seppänen, A., Duncan, S., et al. (2006). Using process tomography as a sensor for optimal control. *Applied Numerical Mathematics*, 56, 1, 37-54